Check for updates

Journal of the American Ceramic Society

RESEARCH ARTICLE OPEN ACCESS

Environmental Barrier Coatings Deposited by Suspension Plasma Spraying

Dapeng Zhou[1,2] | Emine Bakan[1] | Yoo Jung Sohn[1] | Weijie Dong[2] | Robert Vassen[1]

[1]Forschungszentrum Jülich GmbH, Institute of Energy and Climate Research, Materials Synthesis and Processing (IEK-1), Jülich, Germany | [2]Taihang National Laboratory, Tianfu District, Chengdu, China

Correspondence: Dapeng Zhou (juelichzhou@gmail.com)

Received: 23 April 2026 | **Revised:** 12 May 2026 | **Accepted:** 19 May 2026

Keywords: deposition temperature | environment barrier coating | microstructure | phase composition | suspension plasma spray | vertical crack

ABSTRACT

Fully crystalline, dense environmental barrier coatings (EBCs) are required to protect SiC-based ceramic matrix composites, which are the advanced structural materials for hot-section components of gas turbines. Thermal spray technologies, which have been widely used for depositing thermal barrier coatings, are also applied to deposit EBCs. Avoiding the segmental cracks is one of the main challenges in depositing thermal sprayed EBCs. In this work, suspension plasma spraying (SPS) was used to deposit EBCs on the SiC substrates. The combustion of an ethanol-based suspension can bring plasma additional enthalpy. As a result of that, extremely high deposition temperatures (above 1200°C) could be achieved. At such high deposition temperatures, fully crystalline crack-free $Yb_2Si_2O_7$ coatings were successfully obtained. However, A relatively high amount of Yb_2SiO_5 phase was observed in the as-sprayed coatings. The high amount of the Yb_2SiO_5 phase was attributed to the high surface ratio of the particles formed during the suspension plasma spray.

1 | Introduction

There is a continuous and intensive demand for better performance, better fuel efficiency, and lower emissions of gas turbine engines [1 2]. This requires higher service temperatures for the hot-section components of gas turbine engines [3–6]. By using thermal barrier coating (TBC)-coated superalloy components along with the cooling technologies, inlet-gas temperatures that are even higher than the melting point of the superalloys can be achieved [3]. However, it is believed that the TBC-coated superalloy components have already reached their limit in terms of service temperature. With this background, SiC-based ceramic matrix composites (CMCs) with higher service temperatures and excellent high-temperature mechanical properties are regarded as effective replacements for superalloys [7 8].

In a dry atmosphere, SiC-based CMCs present excellent oxidation resistance due to the formation of a dense SiO_2 scale [9]. However, in the presence of water vapor, which is one of the main products of combustion, severe silica volatilization caused by water vapor can lead to accelerated degradation of the CMC components [10]. The recession rate of SiC can be several μm/h which is unacceptable for the applications in gas turbines [11]. The water vapor corrosion can be effectively addressed by applying dense, crack-free environmental barrier coatings (EBCs) on CMCs as a volatilization barrier [3]. Several kinds of ceramic materials such as mullite and barium-strontium-alumino-silicate (BSAS) have been developed as early-generation EBCs. More recently, rare earth silicates, for example, $Yb_2Si_2O_7$ (YbDS) with an even better water vapor stability attracted a lot of interest as a candidate for EBCs [12, 13].

This is an open access article under the terms of the Creative Commons Attribution License, which permits use, distribution and reproduction in any medium, provided the original work is properly cited.
© 2026 The Author(s). *Journal of the American Ceramic Society* published by Wiley Periodicals LLC on behalf of The American Ceramic Society.

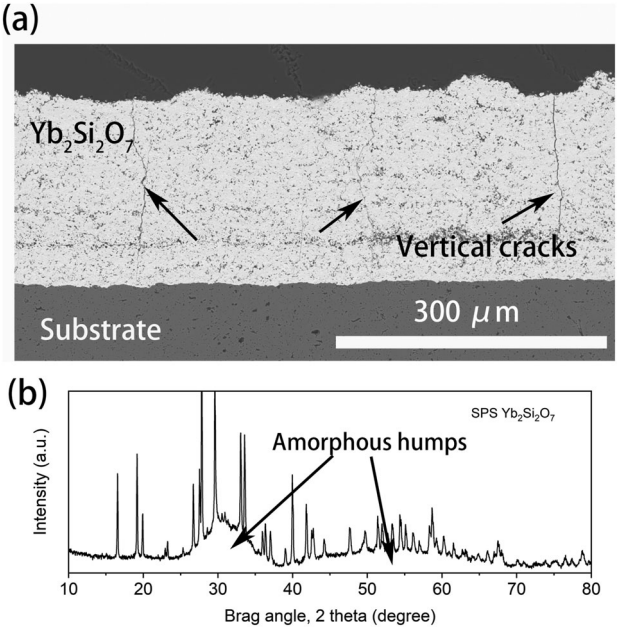

FIGURE 1 | SEM image on the cross-sectional microstructure of as-sprayed SPS YbDS coatings with vertical cracks (a) and XRD pattern on the as-sprayed SPS YbDS coating (b).

Until now, different thermal spraying technologies, such as atmospheric plasma spraying (APS), Very low-pressure plasma spraying (VLPPS), suspension plasma spraying (SPS) and high-velocity oxy-fuel (HVOF) have been applied to deposit EBCs [14–17]. Among them, SPS is a relatively new thermal spray technology using suspension instead of powder as a feedstock. It has a high versatility in coating microstructures, namely coatings with homogeneous microstructure, segmentation cracked microstructure and even columnar microstructure can be obtained [18–23]. By using sub-micro-sized feedstock, SPS splats normally have diameters in the range of 0.5–3 μm [24]. As all the fine particles can be well melted, the splats have a good attachment with each other reducing the number of interlamellar cracks which are often observed in typical APS microstructures [25]. This is beneficial to reduce porosity, aiming for a dense microstructure. As there are no interlamellar cracks to release thermal stress, EBCs sprayed with SPS are prone to a higher stress level. These SPS EBCs are more prone to form vertical cracks than other thermal spray technologies. EBCs sprayed by the SPS typically have a high amorphous content and vertical segmental cracks, as shown in Figure 1. The amorphous phase is mainly formed by the extremely quick solidification rate of the molten ceramic droplets upon impacting the relatively cold substrate. The amorphous phase typically has a large thermal expansion mismatch with the crystalline phase and the SiC substrate [26]. Moreover, the formed amorphous phase can transform into a crystalline phase with a volume change at elevated temperatures. Both factors can introduce a high-stress level, resulting in cracks and even spallation at service [27]. Therefore, the amorphous phase is not desired in EBCs. To obtain a fully crystalline coating, a high deposition temperature above the glass transformation point is necessary [28].

In addition to the amorphous phase issue, getting a dense and air-tight coating is another challenge for thermal sprayed EBCs. Interconnected pores and cracks can provide pathways for water vapor intrusion. Especially the segmentation cracks, as marked in Figure 1, are detrimental to the airtightness of the coating leading to rapid degradation of the underlying substrates [29]. Based on the model developed by Thouless et al., the tensile stresses in the coating ($\sigma_{coating}$) are the driving forces for the segmental cracks [30, 31]. Once the tensile stress exceeds a critical level which is determined by the fracture toughness and thickness of the coating, vertical cracks can be introduced into the coating. The tensile stress which is composed of quenching stress and thermal misfit stress can be roughly estimated with the following equation:

$$\sigma_{coating} = \frac{E_{YbDS}\alpha_{YbDS}\left(T_{melt}-T_{dep}\right)}{1-\upsilon_{YbDS}} + \frac{E_c\left(\alpha_{YbDS}-\alpha_{SiC}\right)\left(T_{dep}-T_R\right)}{1-\upsilon_{YbDS}} \quad (1)$$

where, E_{YbDS} is the elastic modulus of the YbDS (180 GPa) [32]; α_{YbDS} is the thermal expansion coefficient of YbDS ($4.8 \times 10^{-6}°C^{-1}$) [32]; T_{melt} is the melting point of YbDS (1850°C); T_{dep} is the deposition temperature of the coating; E_c is the elastic modulus of the coating; α_{SiC} is the thermal expansion coefficient of the SiC substrate ($4.5 \times 10^{-6}°C^{-1}$) [32]; T_R is the room temperature (25°C); υ_{YbDS} is the Poisson's ratio of YbDS (0.25). It should be noticed that this equation usually gives an overestimation of the stress level, as the stress relaxation contributed by the plastic deformation, creep and defects such as cracks and pores is not considered. However, it can shed light on the ways how to decrease the tensile stress in the coating. The key to avoid vertical cracks is to keep the tensile stress level below the critical level. As the thermal misfit between the YbDS and the SiC is very limited, the thermal misfit stress between the coating and the substrate can be ignored in this case. The tensile stress level is mainly dominated by thermal quenching stress. Specifically, it is determined by the difference between the melting point of YbDS and the deposition temperature. A higher deposition temperature can help to reduce the tensile stress in the coating [33].

By using ethanol-based suspension, additional enthalpy can be obtained by combusting ethanol. This gives SPS an advantage in maintaining a higher deposition temperature than APS [34]. In this work, EBCs were deposited with SPS. The microstructure and phase composition of the coating were investigated. Compared with EBCs obtained with other thermal spraying technologies, an extremely high amount of Yb_2SiO_5 (YbMS) was found in the as-sprayed SPS EBCs. The formation mechanism of the YbMS phase was discussed.

2 | Experiment

2.1 | Materials

YbDS suspension provided by Oerlikon Metco Inc. (Westbury, New York, USA) was used. The suspension was diluted with Ethanol to 5 wt.%. Afterward, the suspension was homogenized on a roller bank for 24 h before using. The morphology of the particles is presented in Figure 2. The particle size was measured with a laser scattered light spectrometer (Horiba LA-950). The

15512916, 2026, 7, Downloaded from https://ceramics.onlinelibrary.wiley.com/doi/10.1111/jace.70976 by Forschungszentrum Jülich GmbH Research Center, Wiley Online Library on [12/08/2026]. See the Terms and Conditions (https://onlinelibrary.wiley.com/terms-and-conditions) on Wiley Online Library for rules of use; OA articles are governed by the applicable Creative Commons License

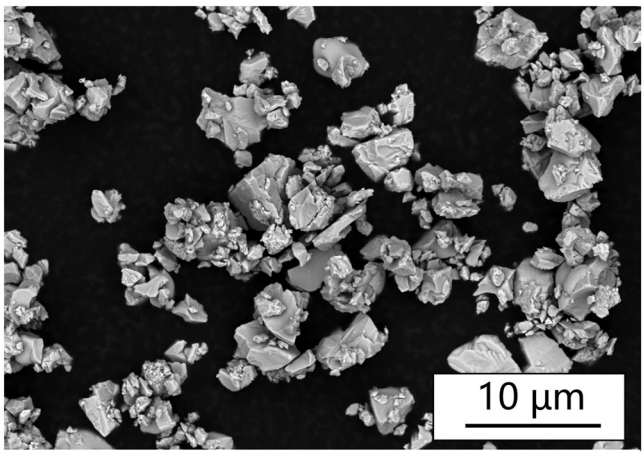

FIGURE 2 | SEM image of the YbDS particles in the as-received commercial suspension.

particle analysis was based on Mie theory. The particles in the suspension had irregular morphologies with a D_{50} size of about 0.8 µm. The dynamic viscosity of the suspension was measured with the Physica MCR 301 rheometer from Anton Paar GmbH. The measured viscosity was 1.55 mPa·s at a shear rate of 10 s^{-1}. Commercial α-SiC plates provided by Saint-Gobain GmbH (Rödental, Germany) were used as substrate. The α-SiC plates were wire cut into pieces with a size of about 20 × 20 × 6 mm^3. Before spraying, the substrate surface was grit blasted with Al_2O_3 (F150). A final surface roughness of about 1.5 µm (Ra) was achieved.

2.2 | Plasma Spraying Conditions

The YbDS coatings were sprayed with an Axial III torch (Northwest Mettech Corporation, Vancouver, Canada) which was mounted on a six-axis robot. The spraying process is schematically illustrated in Figure 3. The SiC substrate was mounted on an Inconel sample holder. To increase the deposition temperature, a short meander with a width of 70 mm and a slow torch raster velocity of 200 mm/s was used. In addition, an infrared pyrometer with a spectral range of 8–11.5 µm was used to monitor the deposition temperatures. Ten data points were collected per second. The emissivity of the deposited coating was assumed to be constant with a value of $\varepsilon = 1$ [35]. In the present study, $\varepsilon = 1$ was adopted as an approximate value to enable consistent comparative temperature measurements during the SPS process. Although the actual emissivity of the coating surface may vary with temperature and surface condition, the measured temperatures are mainly used for relative comparison among different spraying conditions. Therefore, the overall trends and conclusions of this work are not significantly affected. The suspension was injected into the plasma flame with a suspension feeding system developed by Forschungszentrum Jülich GmbH [36]. The schematic of the feeding system is illustrated in Figure 3b. The suspension and ethanol tanks were connected with a compressed air supply. By adjusting the air pressure, the flow rate of the suspension can be obtained in the range of 40–125 g/min. To investigate the particle size distribution and phase composition of the re-solidified particles, the molten YbDS droplets were sprayed into a stainless-steel barrel. The bottom of

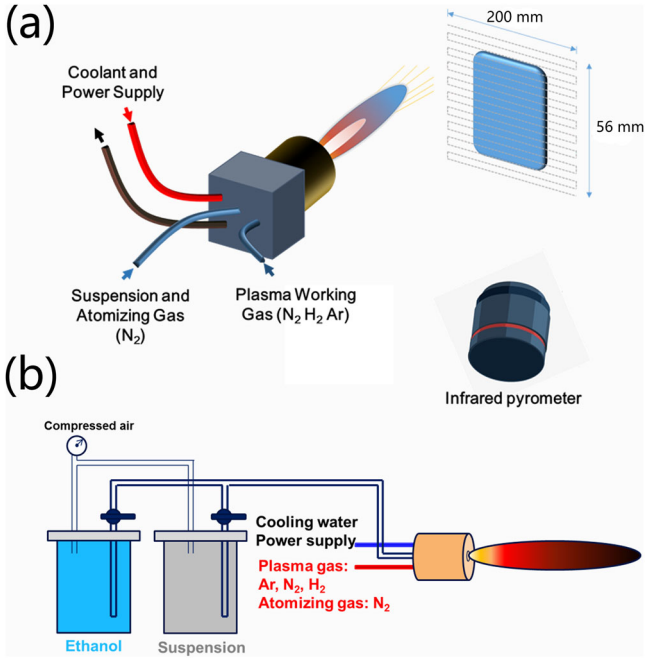

FIGURE 3 | Schematic illustration of the suspension plasma spraying deposition approach of the EBCs deposited at high deposition temperature (a) and the schematic illustration of the suspension feeding system developed by Forschungszentrum Jülich GmbH (b)

the barrel was covered with wet cotton tissues. Once the molten droplets impacted the wet tissue, they quickly solidified. Due to the strong gas flow and high deposition temperature, the molten particles could not be collected at the same spraying distance as the coating process. To reduce the deposition temperature, the spraying distance was increased to 500 mm, as listed in Table 1. In addition, the torch velocity was increased to 1000 mm/s. The meander width was increased to 500 mm. After spraying, the cotton tissues were washed with distilled water to collect the re-solidified particles. Afterward, the collected particles were embedded and metallographically polished.

2.3 | Characterization

The phase composition of the as-sprayed coatings was investigated with a Bruker D4 Endeavor diffractometer using a Cu Kα anode (operating voltage 40 kV, current 40 mA, step size 0.02°, step time 0.75 s). XRD diffraction peaks were deconvolved using Rietveld Analysis (TOPAS Software, Brucker AXS GmbH, Karlsruhe, Germany) for quantitative analysis. Metallographic cross-sections of the coatings were also prepared to investigate the microstructure of the coatings via Scanning Electron Microscope (SEM, ULTRA 55, Carl Zeiss NTS GmbH, Oberkochen, Germany; TM3000). The porosity of the coating was measured by image analysis with the Image J software (Image J 1.53e, open source). Five images of the as sprayed coating covering an area of 85 × 60 μm^2 were used for image analysis. The particle size distribution of the collected resolidified particles was also analyzed with image analysis. To ensure enough particles were counted, SEM images with a view area of 85 × 60 μm^2, including hundreds of particles were analyzed. As the strong contrast between the particles and the resin in the SEM image, the particles can be

15512916, 2026, 7, Downloaded from https://ceramics.onlinelibrary.wiley.com/doi/10.1111/jace.70976 by Forschungszentrum Jülich GmbH Research Center, Wiley Online Library on [12/08/2026]. See the Terms and Conditions (https://onlinelibrary.wiley.com/terms-and-conditions) on Wiley Online Library for rules of use; OA articles are governed by the applicable Creative Commons License

TABLE 1 | Detailed spraying parameters for the environmental barrier coatings and resolidified particles.

Sample ID	Input power (kW)	Current (A)	Coating program	Spraying distance (mm)	Plasma gas composition (slpm)	Feeding rate (g/min)	Raster speed of torch (mm/s)	Preheating cycles	Coating cycles
A	92.4	220	70 × 14 × 2	70	N_2(183.8),H_2 (36.8) Ar (24.5)	123	200	3	2
B	92.4	220	70 × 14 × 2	70	N_2(183.8), H_2 (36.8) Ar (24.5)	90	200	3	5
C	92.4	220	70 × 14 × 2	70	N_2(183.8), H_2 (36.8) Ar (24.5)	65	200	3	30
D	92.4	220	500 × 14 × 2	500	N_2(183.8), H_2 (36.8) Ar (24.5)	123	1000	—	—
E	92.4	220	500 × 14 × 2	500	N_2(183.8), H_2 (36.8) Ar (24.5)	90	1000	—	—
F	92.4	220	500 × 14 × 2	500	N_2(183.8), H_2 (36.8) Ar (24.5)	65	1000	—	—

easily distinguished with image analysis [37]. To improve statistic accuracy, any particles touching the edges of the image were excluded from the analyses. The SEM images, which are two-dimensional (2D), gave the size of particles intersecting with a plane. Seldom, the plane could intersect the diameter of the particles. Therefore, the particle size counted from the 2D images usually gives an underestimation of the particle size. To estimate the three-dimensional (3D) particle size distribution, a stereological unfolding procedure called Schwartz–Saltykov (SS) technique is used [38 39]. As the collected particles had the same spherical geometry but different sizes, so-called polydispersal system, the particle size distribution can be simplified as a superposition of a number of monodispersed systems with given particle sizes. To further simplify the stereological procedure, a log-normal particle size distribution was assumed. The particle size was counted in twenty sections ranging from 0.1 μm to 10 μm with a geometric section scale. Each section of particle size was produced from the random intersection of a plane with the particles. In addition, the largest measured particle size was assumed to represent the largest particle size in the sample. The particles in the largest section could only be produced from the largest particles. Smaller sections could be produced from small particles or any particles larger than that particular section. Each section interval was $10^{-0.1}$ times of the last section. The intersection probabilities of particles in different particle sections are given in Ref. [38].

The 3D particle number of section $i(N_{3Di}; i = 1, 2, \ldots 20)$ can be estimated with the following equation:

$$N_{3Di} = \frac{1}{P_1}\left(N_{2Di} - \sum_{j=1}^{i-1} P_{j+1} N_{3D(i-j)}\right) \tag{2}$$

wherein N_{2Di} was the counted 2D particle number of section i; P_{j+1} was the intersection probabilities of section $j + 1$.

Under the SEM view, the contrast difference among particles indicates their difference in Si content. YbMS phase with a lower Si content showed a bright contrast. It is also possible to get the particle size distribution of the YbMS phase by carefully setting the contrast threshold. The tricky thing was how to determine the threshold of YbMS phase. According to the Delesse principle, the volume fraction of a particular component in a 3D structure is equal to the area fraction it occupies in a 2D section [40]. The area ratio of YbMS phase to the total detected particle area should be the same as the phase ratio measured with XRD. Therefore, the threshold of YbMS phase was calibrated the XRD results.

3 | Results and Discussion

By varying suspension feeding rates, EBC samples A–C were prepared. The main spraying parameters are listed in Table 1. The typical profile of the measured deposition temperature is presented in Figure 4. The fluctuation of the temperature was in step with the movement of the torch. The samples were preheated with plasma flame for three cycles. With preheating, the substrate temperature was quickly increased above 800°C. Afterward, the suspension was injected with a feeding rate of 90 g/min into the plasma flame. With the injection of suspension, the deposition temperature was further increased to above 1200°C. Generally, the coating process can be divided into three phases: preheating phase, coating phase, and cooling phase. Assuming the output power of the torch was constant for each phase, and the radiative power of the heated sample was limited, the sample can be treated as heated by a thermostatic surrounding. The heating rate was proportional to the difference between the surrounding temperature and the sample temperature. The surrounding temperature is equal to the equilibrium temperature of the sample. The temperature of the sample as the function of heating time could be estimated based on Newton's heating law as described in the Equation (3) [41].

$$T(t) = T_b - (T_b - T_0)\, e^{-at} \tag{3}$$

where, $T(t)$ is the temperature of the sample at time t; T_b is the equilibrium temperature of the sample; T_0 is the surrounding temperature (25°C); a is a positive constant which can be obtained by fitting the temperature line; e is the Euler's number. By fitting the temperature profile of the pre-heating and the coating phases

15512916, 2026, 7, Downloaded from https://ceramics.onlinelibrary.wiley.com/doi/10.1111/jace.70976 by Forschungszentrum Jülich GmbH Research Center, Wiley Online Library on [12/08/2026]. See the Terms and Conditions (https://onlinelibrary.wiley.com/terms-and-conditions) on Wiley Online Library for rules of use; OA articles are governed by the applicable Creative Commons License

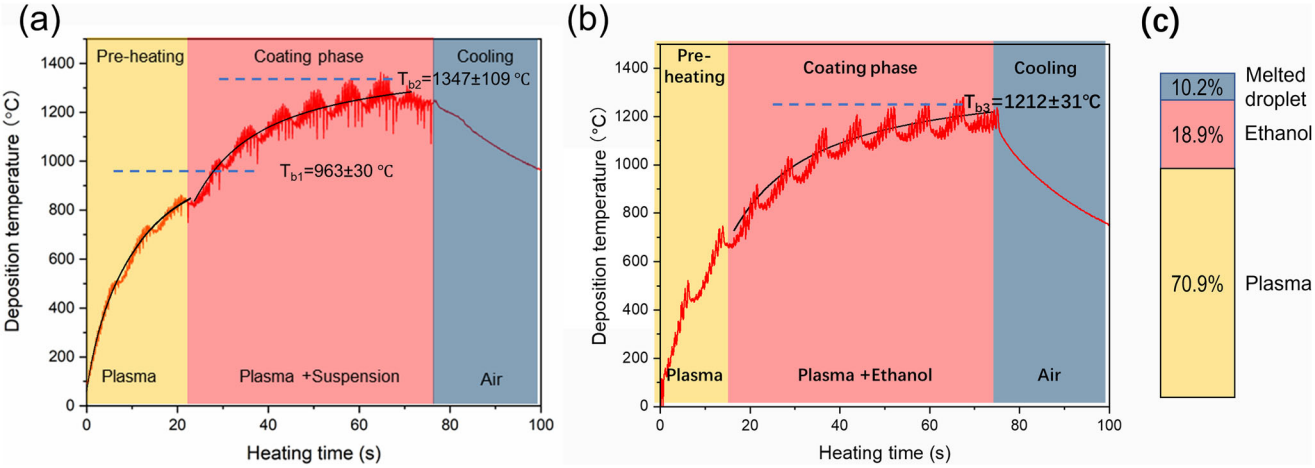

FIGURE 4 | Deposition temperature profile of the samples by injecting suspension (a) and ethanol (b); the estimated power contribution (c).

the equilibrium temperature of the samples at different phases can be obtained, as marked by the dashed line in Figure 4. The equilibrium temperature of the preheating (T_{b1}) was 963 ± 30°C; while the equilibrium temperature of the coating phase (T_{b2}) was 1347 ± 109°C. By injecting suspension, the equilibrium temperature of the heated sample was increased by 384°C. The injected suspension was an ethanol-based suspension. The combustion of ethanol could introduce additional enthalpy which can help to increase the output power of the torch leading to a higher deposition temperature. In addition to this, the deposited molten ceramic droplets with an extremely high temperature could also bring additional heat transfer resulting in a higher deposition temperature [42]. To clarify which was the dominant factor for the increased deposition temperature, pure ethanol with a feeding rate of 90 g/min was also injected. The temperature profile with injecting ethanol is presented in Figure 4b. By fitting the line with Equation (3), the estimated steady-state temperature (T_{b3}) of the substrate was 1212 ± 31°C. As only pure ethanol was injected, it is expected that the increase in the steady-state temperature with a value of 245°C was exclusively contributed by the combustion of ethanol.

According to the Newton's law of heating, the heating power (P) is proportional to the difference between the equilibrium temperature (T_b) and surrounding temperature (T_0) as described in Equation (4) [43]:

$$P = kA\,(T_b - T_0) \tag{4}$$

where, A is the surface area of the sample, k is the heat transfer coefficiency (assumed independent of the sample temperature). Assuming the kA value was the same for injecting ethanol or suspension, it can easily get that the heating power was proportional to the temperature difference $T_b - T_0$. Based on this, the contribution ratio of the total heating power from different heating sources could be estimated, as indicated in Figure 4c. The primary source of heating power was derived from the plasma, contributing approximately 70.9%. Additional enthalpy, resulting from the combustion of ethanol, accounted for about 18.9% of the total heating power. In addition, molten droplets contributed 10.2% to the overall heating power. The combustion of ethanol was the main reason for the further increased deposition temperature.

Microstructures of the as-sprayed coatings with different suspension feeding rates are presented in Figure 5. Images with a higher magnification are also shown in the upper corner to give a general view of the microstructure of the as-sprayed coatings. The as-sprayed coatings A–C had a thickness of 100 μm, 234 μm, and 298 μm, respectively. No segmentation cracks were observed in all as-sprayed coatings. By increasing the deposition temperature, segmentation cracks, which are often observed in as-sprayed coatings were successfully avoided. With different suspension feeding rates, the as-sprayed coating showed different porosity levels. Sample A deposited with the highest suspension feeding rate (123 g/min) showed the highest porosity level with a value of 34.9 ± 3.5%. A large number of pores with sizes of several micrometers can be observed from the cross-section. Some particles with irregular geometries were also observed. This indicates that the particles were not well melted. By reducing the feeding rate to 90 g/min, the porosity level of sample B was decreased to 13.7 ± 1.6%. Unmelted particles were not observed from the cross-section, but the coating still showed a high porosity level. With the lowest feeding rate (65 g/min), sample C showed the lowest porosity value of 5.3 ± 1.3% with a relatively dense microstructure.

XRD patterns of the as-sprayed coatings and the raw powder are presented in Figure 6. Compared with SPS coatings deposited at a low deposition temperature, as shown in Figure 1, no amorphous phase was found in all as-sprayed coatings. Fully crystalline EBCs were successfully obtained. With a high deposition temperature, the cooling rate of droplets was slowed, giving atoms more time and mobility to organize into a more thermodynamically favorable crystalline phase [44]. Only the β-$Yb_2Si_2O_7$ (YbDS) phase (PDF number 01-082-0734) was detected in the raw powder. The same YbDS phase was also found in all the as-sprayed coatings as the main phase. In addition to the YbDS phase, the Yb_2SiO_5 phase (PDF number 00-040-0368) as the secondary phase was detected in all the as-sprayed coatings. The Yb_2SiO_5 (YbMS) phase has characteristic peaks in the Bragg angle range of 13°–16° (marked with a dashed circle in Figure 6). With a reduced feeding rate, the intensity of the characteristic peaks significantly increased,

15512916, 2026, 7, Downloaded from https://ceramics.onlinelibrary.wiley.com/doi/10.1111/jace.70976 by Forschungszentrum Jülich GmbH Research Center, Wiley Online Library on [12/08/2026]. See the Terms and Conditions (https://onlinelibrary.wiley.com/terms-and-conditions) on Wiley Online Library for rules of use; OA articles are governed by the applicable Creative Commons License

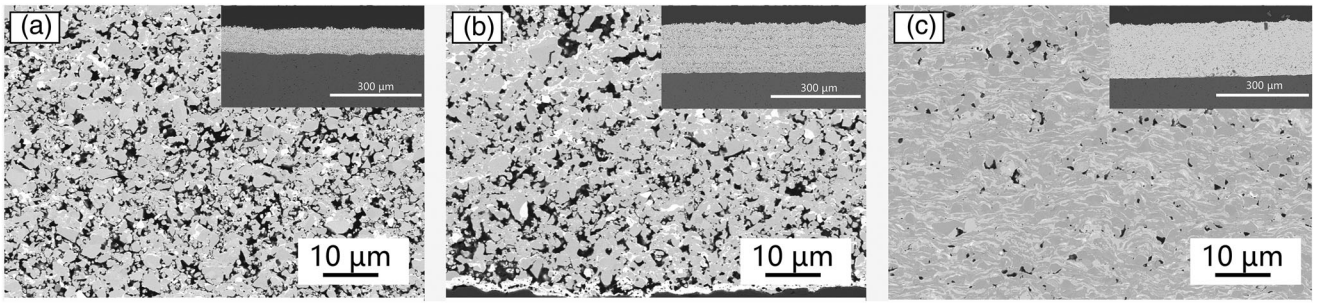

FIGURE 5 | Microstructure of the as-sprayed coatings which were sprayed with different suspension feeding rates (a) 123 g/min, (b) 90 g/min and 65 g/min (c).

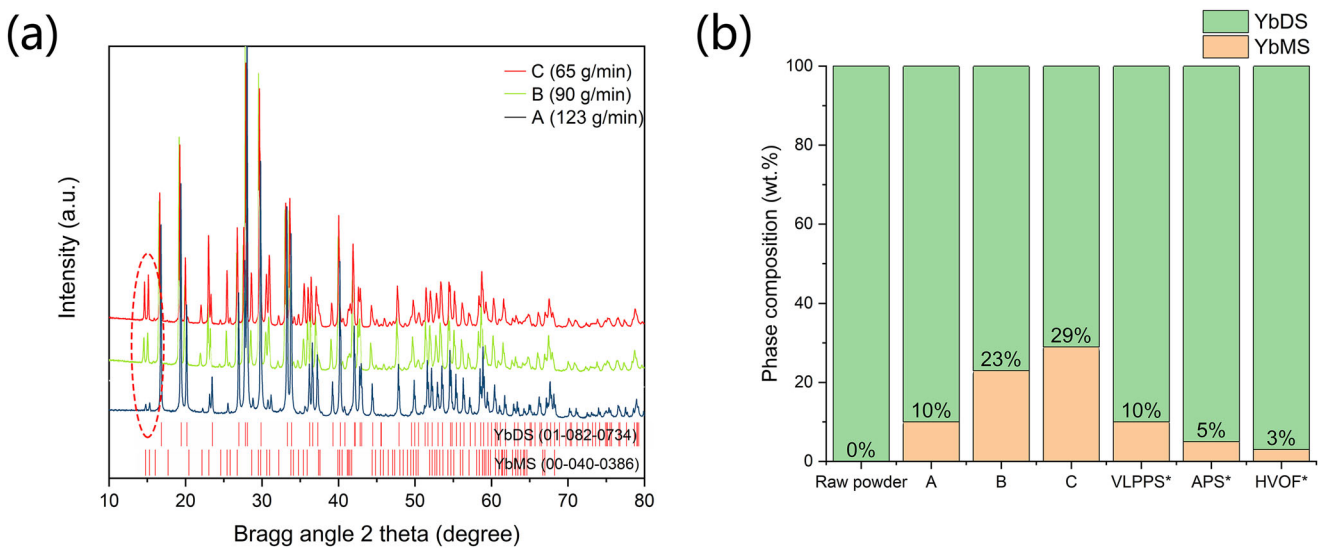

FIGURE 6 | XRD patterns of the raw powder and the as-sprayed coatings with different feeding rates (a); phase composition of the as sprayed EBCs deposited with SPS, VLPPS, APS and HVOF; * cited from Reference (b) [14].

indicating an increase in the amount of YbMS. Phase composition of the as-sprayed coatings was obtained by quantitative phase analysis. As shown in Figure 6b, samples A, B, and C contained about 10, 23, and 29 wt.% of YbMS, respectively, with the balance being YbDS. Due to Si loss of the molten YbDS particles during the spraying flight, YbMS phase is also observed in EBCs deposited by APS, VLPPS, and HVOF [14 45]. Typically, the ratio of the YbMS phase in APS EBCs is below 5%. However, the Yb_2SiO_5 ratio in the as-sprayed SPS EBCs was much higher than 10%. In the case of a low feeding rate, for example, the Yb_2SiO_5 ratio of sample C could be as high as 29%, which was much higher than that of the typical APS EBCs. However, regardless of the extremely high Yb_2SiO_5 content, no Yb_2O_3 phase, which is the typical product after a further loss of Si from Yb_2SiO_5 was found in the as-sprayed coatings. Compared with $Yb_2Si_2O_7$, Yb_2SiO_5 generally exhibits a higher coefficient of thermal expansion (~6–8 × 10^{-6} K^{-1}), which may result in a larger thermal expansion mismatch between the coating and the SiC-based substrate. Consequently, higher thermally induced stresses may develop during thermal cycling, potentially affecting the long-term cyclic durability of the coating system. On the other hand, previous studies have shown that Yb_2SiO_5 possesses superior water vapor corrosion resistance compared with $Yb_2Si_2O_7$. Therefore, it is difficult to draw a simple conclusion regarding whether a higher amount of Yb_2SiO_5 is entirely beneficial or detrimental to the overall thermal cycling lifetime of the coating, since both thermomechanical compatibility and environmental durability must be considered simultaneously.

To better show the distribution of the YbMS phase, more detailed microstructures of the as sprayed coating are presented in Figure 7. The coatings were mainly composed of two phases with different contrast under SEM. EDS was carried out on the points marked with numbers. The results showed that the relatively brighter phase had a lower Si content, while the relatively darker phase showed a higher Si content. This indicates that the brighter phase was the YbMS phase. With a decrease in the suspension feeding rate, the amount of the YbMS phase increased. Sample C showed an extremely high amount of YbMS phase. These observations are well consistent with the XRD results.

To investigate the formation mechanism of the exceptionally high amount of YbMS phase in the SPS EBCs, resolidified particles were collected with varying feeding rates, as detailed in Table 1. When the molten droplets impacted on the wet tissues, the cooling rate of the particles would be extremely high. The atoms

15512916, 2026, 7, Downloaded from https://ceramics.onlinelibrary.wiley.com/doi/10.1111/jace.70976 by Forschungszentrum Jülich GmbH Research Center, Wiley Online Library on [12/08/2026]. See the Terms and Conditions (https://onlinelibrary.wiley.com/terms-and-conditions) on Wiley Online Library for rules of use; OA articles are governed by the applicable Creative Commons License

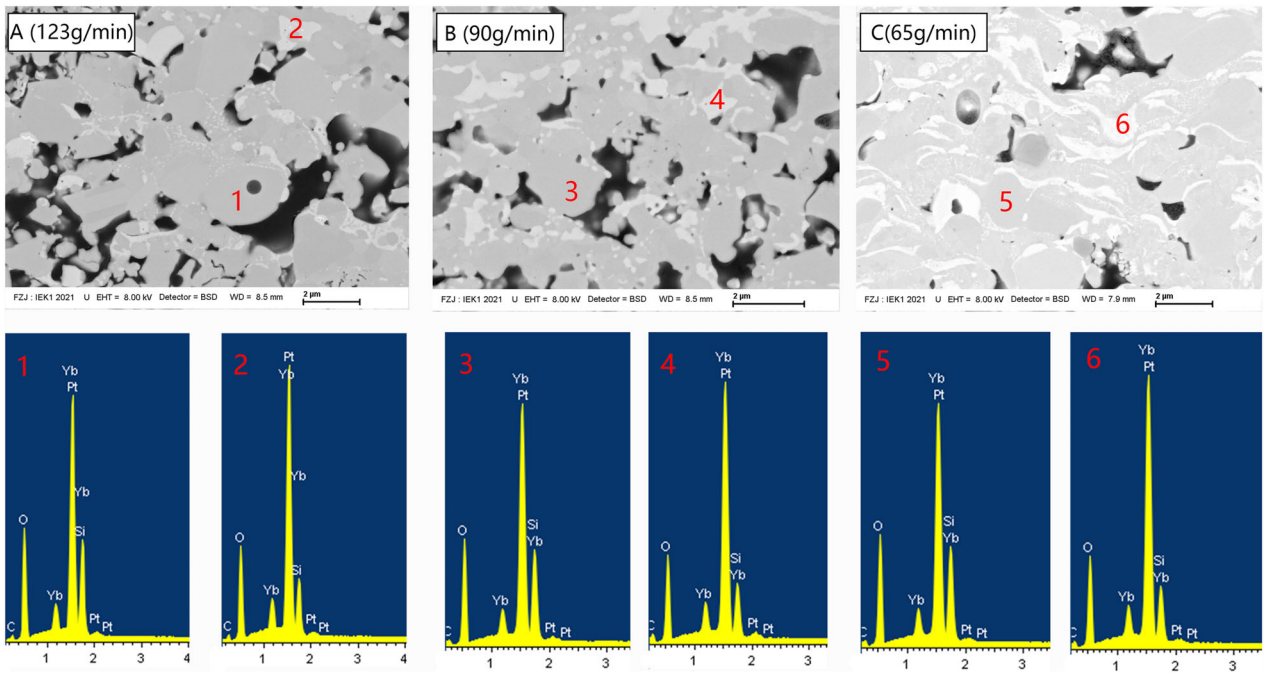

FIGURE 7 | Cross-section microstructure of the coatings sprayed with different suspension feeding rates and corresponding energy dispersive spectroscopy (EDS) at the points marked with numbers.

have insufficient time to reach the thermodynamic equilibrium. It would be expected that the obtained solidified particles had the same chemical composition and chemical distribution as the molten droplets.

The cross-sectional microstructure of the resolidified particles collected at different suspension feeding rates is presented in Figure 8 (Samples D to F). Most of the particles showed a round cross-section profile, which was a typical morphology of the resolidified particles. This indicates that most of the particles were well-melted during the coating process. All the particles were well polished. However, some particles were pulled out during the metallography preparation. The positions of the missing particles are marked with red arrows in Figure 8. The missing particles could lead to errors in the statistical results. As the number of missing particles was limited compared with the total counted particle number, it is assumed that the effect of the missing particles was limited. To better show the details of the particles, SEM images with higher magnification are posted in the up-right corner. As the SEM images were obtained with a backscattered electron detector, the contrast difference of particles was mainly contributed by the chemical composition difference, specifically the difference of the Si content. While particles showed significant differences in contrast between different ones, areas within the single particle showed the same contrast. This indicates that the chemical composition within one particle was quite homogeneous.

The counted particle numbers in each particle size section are presented in Figure 9 (Samples D to F). As mentioned before, the particle size measured from 2D images usually gives an underestimation on the particle size. To get a more accurate particle size distribution, a stereological unfolding procedure Schwartz–Saltykov (SS) technique mentioned above was used. The estimated 3D particle number in each section is presented in Figure 9 (Samples D1 to F1). By knowing the particle number in each section, the volume ratio of each particle section can be calculated. The calculated results are listed in the Figure 9 (Samples D2 to F2). The resolidified powder samples D, E and F were collected with a feeding rate of 65 g/min, 90 g/min and 123 g/min. Samples D, E and F had a volumetric D_{50} size of 4.6 μm, 4.0 μm and 3.1 μm, respectively. With the reduction of the suspension feeding rate, the D_{50} size of the collected powder was reduced, gradually. The atomizing flow rate was fixed at 15 SLPM. With a reduction of the suspension feeding rate, the gas-suspension ratio was increased. This facilitated the atomization of the suspension, leading to smaller droplets and ceramic particles [46, 47].

As discussed before, the contrast of the particle indicates the Si difference. Particles with a lower Si content showed a brighter contrast. It was assumed below a certain threshold, the particles were YbMS phase. The threshold was calibrated with XRD results to make sure that the area ratio of the YbMS particles to the total particle area was consistent with the YbMS phase ratio which was measured with XRD. The particle size distribution of the YbMS phase is presented in Figure 9 (Samples D2 to F2). The YbMS particles showed a smaller particle size compared with YbDS particles. No YbMS particles with a size larger than 5 μm were found. In addition, the particle size section with a small size had a higher ratio of YbMS phase. This indicates that smaller particles were more easily lost SiO_2 forming the YbMS phase during the coating process.

SiO_2 loss of YbDS is often observed in the thermal sprayed EBCs, as the volatilization of the SiO_2 [27]. The process is described by Equation (5). In addition, water vapor could be introduced into the plasma flame by the burning of Ethanol. It would be expected that the introduced water vapor might react with the YbDS producing gaseous Si-containing products, as described in

15512916, 2026, 7, Downloaded from https://ceramics.onlinelibrary.wiley.com/doi/10.1111/jace.70976 by Forschungszentrum Jülich GmbH Research Center, Wiley Online Library on [12/08/2026]. See the Terms and Conditions (https://onlinelibrary.wiley.com/terms-and-conditions) on Wiley Online Library for rules of use; OA articles are governed by the applicable Creative Commons License

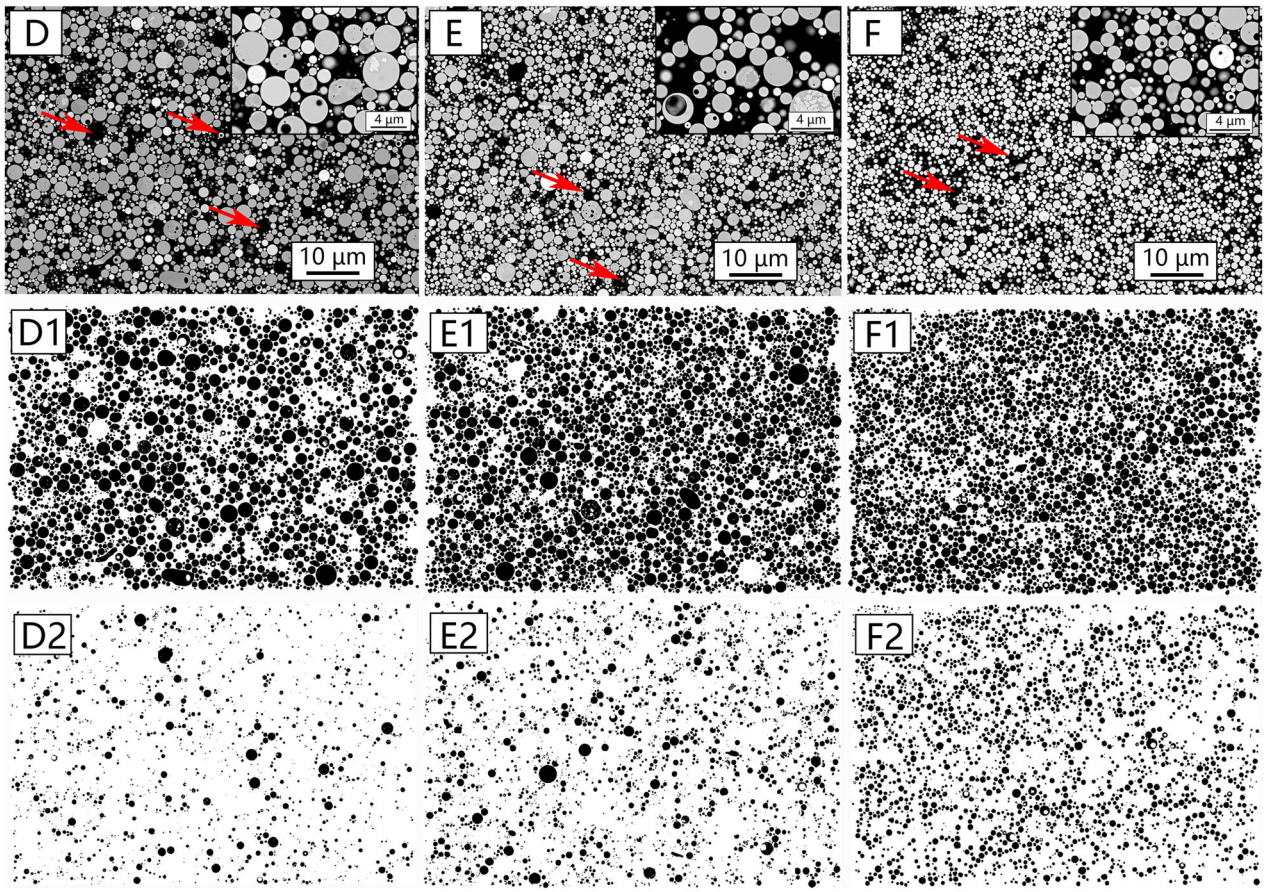

FIGURE 8 | SEM images of the resolidified particles collected at different suspension feeding rates: D (123 g/min), E (90 g/min), and F (65 g/min); Monochrome images of the resolidified particles collected at different suspension feeding rates: D1 (123 g/min), E1 (90 g/min), and F1 (65 g/min); Monochrome images of the estimated YbMS phase collected at different suspension feeding rates: D2 (123 g/min), E2 (90 g/min), and F2 (65 g/min).

Equation (6) [48]. This reaction would further deplet SiO_2 from YbDS leading to the formation of YbMS in the particle. SiO_2 volatilization and water vapor corrosion might both contribute to the depletion of SiO_2 in molten particles. However, further study is needed to clarify which was the dominant reason for the Si depletion of SPS particles.

$$Yb_2Si_2O_7 \rightarrow Yb_2SiO_5 + SiO_2\,(g) \tag{5}$$

$$Yb_2Si_2O_7 + H_2O\,(g) \rightarrow Yb_2SiO_5 + Si(OH)_4\,(g) \tag{6}$$

Both volatilization and water vapor corrosion are temperature dependent processes, the reaction rate coefficients of both follow an Arrhenius behavior [49]. In other words, higher particle temperature could accelerate Si depletion leading to a higher YbMS ratio within a certain particle flight time in the plasma flame. Assuming the particles had a uniform temperature distribution, the heating up rate of the particles can be estimated with the following Equation (7) [50]:

$$\frac{dT_p}{dt} = \frac{6Q}{\pi {d_p}^3 \rho_p C_{ps}} \propto \frac{1}{d_p} \tag{7}$$

where, Q is the instant heat transfer from plasma to the particle; d_p is the particle size; ρ_p is the particle density; C_{ps} is the specific heat capacity of the particle. As the instant heat transfer was proportional to the square of the particle size, it can be calculated that the heating-up rate of the particle was inversely proportional to the particle size. This means that smaller particles could reach a higher temperature with the same flight time as larger particles. In addition to the higher particle temperature, a smaller particle had a higher specific surface area (SSA), as seen in Equation (8). A higher SSA could also accelerate the SiO_2 depletion of the particles during the flight. In summary, the smaller particles had a higher particle temperature and a higher SSA. Both factors contributed to the high ratio of YbMS for smaller particles. Compared with VLPPS, APS, and HVOF, which have particle sizes of tens of micrometers, the particle size of SPS was only several micrometers. The extremely small particle size of the SPS might be the reason for the extremely high YbMS phase ratio of the SPS EBCs.

$$SSA \propto \frac{1}{d_p} \tag{8}$$

To better show the formation process of the YbMS phase in SPS EBCs, the heating history of the particles in SPS is described in Figure 10. After being injected into the plasma flame, the suspension was first atomized into small liquid droplets. Afterward, the ethanol was quickly combusted, introducing additional enthalpy and water vapor into the flame. Consequently, the remaining ceramic particles were heated and accelerated by the plasma flame toward the substrate. Both volatilization and water vapor corrosion might contribute to the SiO_2 depletion of the YbDS

15512916, 2026, 7, Downloaded from https://ceramics.onlinelibrary.wiley.com/doi/10.1111/jace.70976 by Forschungszentrum Jülich GmbH Research Center, Wiley Online Library on [12/08/2026]. See the Terms and Conditions (https://onlinelibrary.wiley.com/terms-and-conditions) on Wiley Online Library for rules of use; OA articles are governed by the applicable Creative Commons License

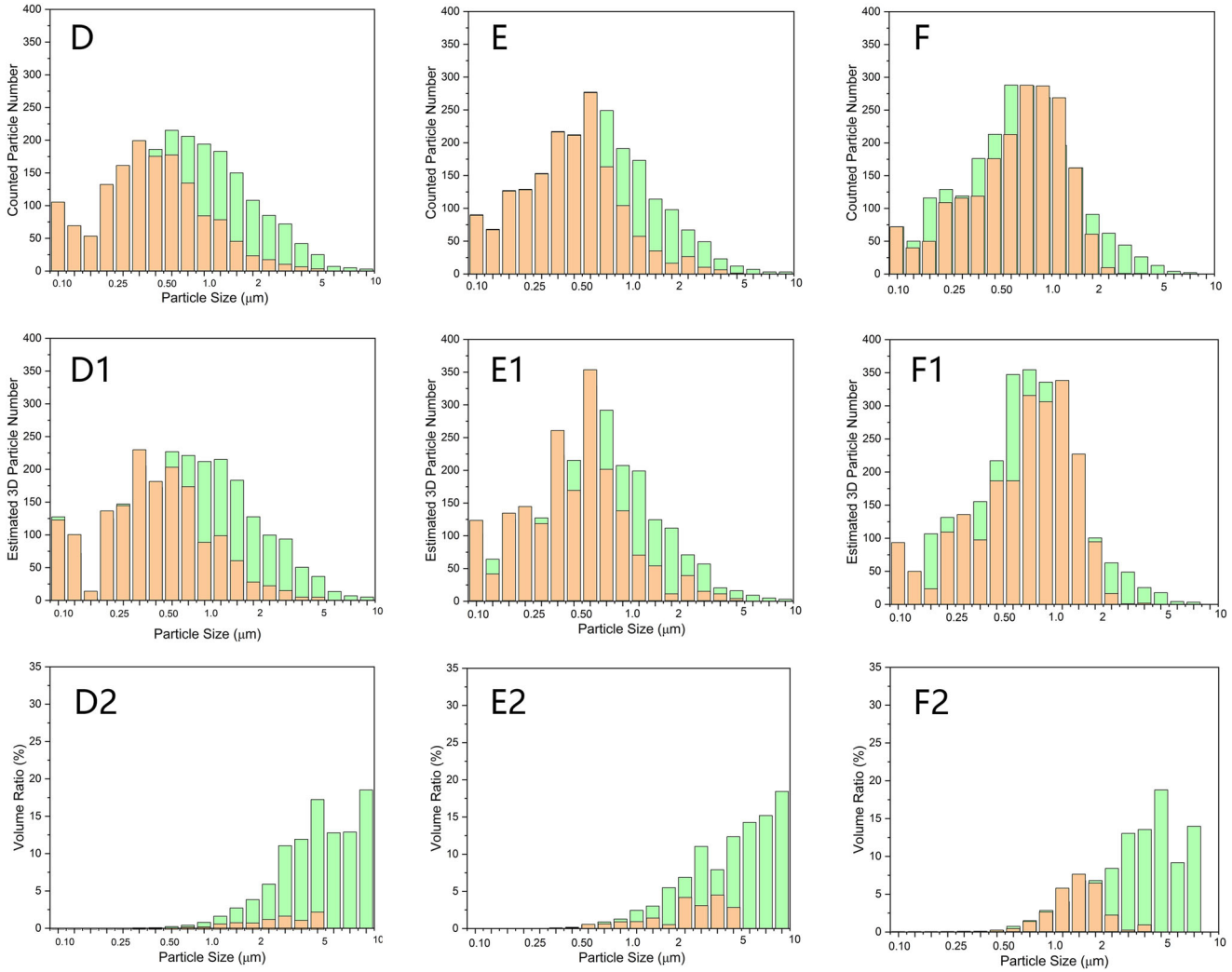

FIGURE 9 | Counted particle size distribution of resolidified powder collected with different suspension feeding rates: D (123 g/min), E (90 g/min), and F (65 g/min); estimated 3D particle size distribution: D1 (123 g/min), E1 (90 g/min), and F1 (65 g/min); volume ratio of particles with different particle size: D2 (123 g/min), E2 (90 g/min), and F2 (65 g/min).

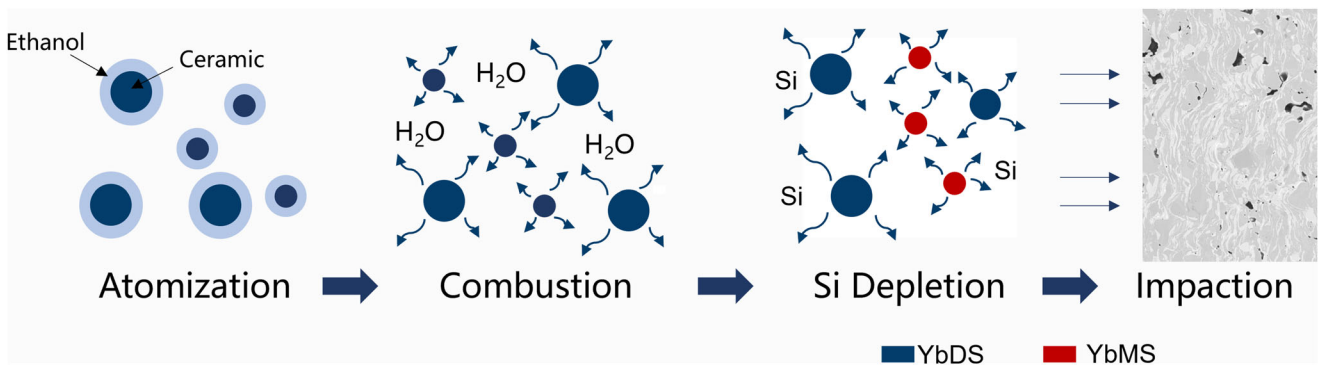

FIGURE 10 | Illustration on the possible particle-surrounding interactions during the suspension plasma spraying.

particles. The smaller particles more easily lost SiO_2 forming YbMS phase. Finally, the molten droplets impact the substrate and solidify to form the coating. Due to the flattening of the droplets, a YbMS/ YbDS lamellar structure was obtained.

4 | Conclusion

EBCs were deposited with SPS. To avoid amorphous phase and segmentation cracks which are typically found in thermal sprayed

15512916, 2026, 7, Downloaded from https://ceramics.onlinelibrary.wiley.com/doi/10.1111/jace.70976 by Forschungszentrum Jülich GmbH Research Center, Wiley Online Library on [12/08/2026]. See the Terms and Conditions (https://onlinelibrary.wiley.com/terms-and-conditions) on Wiley Online Library for rules of use; OA articles are governed by the applicable Creative Commons License

EBCs extremely high deposition temperatures were utilized in this work. The main conclusions are as follows:

1. Fully crystalline, segmentation crack-free YbDS EBCs were successfully obtained by suspension plasma spraying at extremely high deposition temperatures.
2. The suspension feeding rate could significantly affect the porosity level and phase composition of the as-sprayed EBCs. With a reduction of the suspension feeding rate, the porosity level of the coating can be reduced. However, a higher ratio of YbMS phase was found at the same time.
3. Both volatilization of SiO_2 and water vapor corrosion might have contributed to the SiO_2 depletion leading to the formation of the YbMS phase. As the smaller particles had higher particle temperature and higher specific surface area, which accelerated the SiO_2 depletion, the smaller particles had a higher YbMS ratio.

Acknowledgments

The authors would like to sincerely acknowledge the contributions of colleagues from their institute: Dr. Georg Mauer for the fruitful discussion, Mr. Frank Kurze and Mr. Karl-Heinz Rauwald for their invaluable assistance with the spraying work, and Mr. Martin Tandler for his professional assistance with the temperature detection.

Open access funding enabled and organized by Projekt DEAL.

Funding

The authors have nothing to report.

Data Availability Statement

The data that support the findings of this study are available from the corresponding author upon reasonable request.

References

1. G. Marin, A. Titov, A. Akhmetshin, and A. Ishalin, "Increasing the Efficiency of a Conversion Gas Turbine Engine by Adding Hydrogen to Fuel Gas," *International Journal of Hydrogen Energy* 97 (2025): 649–656, https://doi.org/10.1016/j.ijhydene.2024.11.304.

2. X. Zhang, X. Zhuo, Z. Fan, et al., "Al_2O_3-modified 7YSZ Thermal Barrier Coatings for Protection Against Volcanic Ash Corrosion," *NPJ Materials Degradation* 6, no. 1 (2022): 89, https://doi.org/10.1038/s41529-022-00308-3.

3. N. P. Padture, "Environmental Degradation of High-temperature Protective Coatings for Ceramic-matrix Composites in Gas-turbine Engines," *NPJ Materials Degradation* 3, no. 1 (2019): 1–6, https://doi.org/10.1038/s41529-019-0075-4.

4. O. Guillon, *Advanced Ceramics for Energy Conversion and Storage* (Elsevier, 2019).

5. E. Bakan, D. E. Mack, G. Mauer, R. Vaßen, J. Lamon, and N. P. Padture, "1 - High-temperature Materials for Power Generation in Gas turbines," in *Advanced Ceramics for Energy Conversion and Storage*, ed. Guillon O, (Elsevier, 2020), 3–62.

6. S.-H. Liu, J. P. Trelles, C.-J. Li, C.-X. Li, and H.-B. Guo, "A Review and Progress of Multiphase Flows in Atmospheric and Low Pressure Plasma Spray Advanced Coating," *Materials Today Physics* 27 (2022): 100832, https://doi.org/10.1016/j.mtphys.2022.100832.

7. N. P. Padture, "Advanced Structural Ceramics in Aerospace Propulsion," *Nature Materials* 15, no. 8 (2016): 804–809, https://doi.org/10.1038/nmat4687.

8. Z.-Y. Wei, G.-H. Meng, L. Chen, et al., "Progress in Ceramic Materials and Structure Design Toward Advanced Thermal Barrier Coatings," *Journal of Advanced Ceramics* 11, no. 7 (2022): 985–1068, https://doi.org/10.1007/s40145-022-0581-7.

9. G. Karadimas and K. Salonitis, "Ceramic Matrix Composites for Aero Engine Applications—A Review," *Applied Sciences* 13, no. 5 (2023): 3017, https://doi.org/10.3390/app13053017.

10. E. J. Opila, D. S. Fox, and N. S. Jacobson, "Mass spectrometric identification of Si–O–H (g) species from the reaction of silica with water vapor at atmospheric pressure," *Journal of the American Ceramic Society* 80, no. 4 (1997): 1009–1012, https://doi.org/10.1111/j.1151-2916.1997.tb02935.x.

11. E. J. Gildersleeve V, E. Bakan, M. Rasinski, et al., "Unveiling Microsecond Diffusion Bonding Phenomena Enabled by Air Plasma Spraying Zirconia Thermal Barrier Ceramics Onto Rare Earth Environmental Barrier Silicates," *Scientific Reports* 15, no. 1 (2025): 27031, https://doi.org/10.1038/s41598-025-12218-w.

12. K. N. Lee, "$Yb_2Si_2O_7$ Environmental Barrier Coatings With Reduced Bond Coat Oxidation Rates via Chemical Modifications for Long Life," *Journal of the American Ceramic Society* 102, no. 3 (2019): 1507–1521, https://doi.org/10.1111/jace.15978.

13. K. N. Lee, D. S. Fox, and N. P. Bansal, "Rare Earth Silicate Environmental Barrier Coatings for SiC/SiC Composites and Si3N4 Ceramics," *Journal of the European Ceramic Society* 25, no. 10 (2005): 1705–1715, https://doi.org/10.1016/j.jeurceramsoc.2004.12.013.

14. R. Vaßen, E. Bakan, C. Gatzen, S. Kim, D. E. Mack, and O. Guillon, "Environmental Barrier Coatings Made by Different Thermal Spray Technologies," *Coatings* 9, no. 12 (2019): 784.

15. E. Bakan, D. Marcano, D. Zhou, Y. J. Sohn, G. Mauer, and R. Vaßen, "Yb2Si2O7 Environmental Barrier Coatings Deposited by Various Thermal Spray Techniques: A Preliminary Comparative Study," *Journal of Thermal Spray Technology* 26, no. 6 (2017): 1011–1024, https://doi.org/10.1007/s11666-017-0574-1.

16. E. J. Gildersleeve and S. Sampath, "Dynamic Interactions of Ingested Molten Silicate Particles With Air Plasma Sprayed Thermal Barrier Coatings," *Journal of Materials Research* 35, no. 17 (2020): 2321–2334, https://doi.org/10.1557/jmr.2020.196.

17. Q. Guo, W. He, J. He, et al., "Characterization of Yb2SiO5-based Environmental Barrier Coating Prepared by Plasma Spray–physical Vapor Deposition," *Ceramics International* 48, no. 14 (2022): 19990–19999, https://doi.org/10.1016/j.ceramint.2022.03.274.

18. D. Zhou, O. Guillon, and R. Vaßen, "Development of YSZ Thermal Barrier Coatings Using Axial Suspension Plasma Spraying," *Coatings* 7, no. 8 (2017): 120, https://doi.org/10.3390/coatings7080120.

19. P. Sokołowski, S. Kozerski, L. Pawłowski, and A. Ambroziak, "The Key Process Parameters Influencing Formation of Columnar Microstructure in Suspension Plasma Sprayed Zirconia Coatings," *Surface and Coatings Technology* 260 (2014): 97–106, https://doi.org/10.1016/j.surfcoat.2014.08.078.

20. A. Akbarnozari, S. Amiri, A. Dolatabadi, and C. Moreau, "Analysis of Scattering Light From in-flight Particles in Suspension Plasma Spray for Size Measurement," *Journal of Thermal Spray Technology* 28, no. 4 (2019): 678–689, https://doi.org/10.1007/s11666-019-00852-6.

21. N. Kumar, S. Mahade, A. Ganvir, and S. Joshi, "Understanding the Influence of Microstructure on Hot Corrosion and Erosion Behavior of Suspension Plasma Sprayed Thermal Barrier Coatings," *Surface and Coatings Technology* 419 (2021): 127306, https://doi.org/10.1016/j.surfcoat.2021.127306.

22. K. Leng, A. Rincon Romero, F. Venturi, I. Ahmed, and T. Hussain, "Solution Precursor Thermal Spraying of Gadolinium Zirconate for

15512916, 2026, 7, Downloaded from https://ceramics.onlinelibrary.wiley.com/doi/10.1111/jace.70976 by Forschungszentrum Jülich GmbH Research Center, Wiley Online Library on [12/08/2026]. See the Terms and Conditions (https://onlinelibrary.wiley.com/terms-and-conditions) on Wiley Online Library for rules of use; OA articles are governed by the applicable Creative Commons License

Thermal Barrier Coating," *Journal of the European Ceramic Society* 42, no. 4 (2022): 1594–1607, https://doi.org/10.1016/j.jeurceramsoc.2021.11.050.

23. D. Zhou, D. E. Mack, P. Gerald, O. Guillon, and R. Vaßen, "Architecture Designs for Extending Thermal Cycling Lifetime of Suspension Plasma Sprayed Thermal Barrier Coatings," *Ceramics International* 45, no. 15 (2019): 18471–18479, https://doi.org/10.1016/j.ceramint.2019.06.065.

24. D. Zhou, *Columnar* Structured Thermal Barrier Coatings Deposited *by* Axial Suspension Plasma Spraying (Forschungszentrum Jülich GmbH, 2019).

25. D. Zhou, J. Malzbender, Y. J. Sohn, O. Guillon, and R. Vaßen, "Sintering Behavior of Columnar Thermal Barrier Coatings Deposited by Axial Suspension Plasma Spraying (SPS)," *Journal of the European Ceramic Society* 39 (2018): 482–490, https://doi.org/10.1016/j.jeurceramsoc.2018.09.020.

26. E. Bakan, M. Kindelmann, W. Kunz, H. Klemm, and R. Vaßen, "High-velocity Water Vapor Corrosion of Yb-silicate: Sprayed vs. sintered Body," *Scripta Materialia* 178 (2020): 468–471, https://doi.org/10.1016/j.scriptamat.2019.12.019.

27. K. N. Lee, D. Zhu, and R. S. Lima, "Perspectives on Environmental Barrier Coatings (EBCs) Manufactured via Air Plasma Spray (APS) on Ceramic Matrix Composites (CMCs): A Tutorial Paper," *Journal of Thermal Spray Technology* 30, no. 1 (2021): 40–58, https://doi.org/10.1007/s11666-021-01168-0.

28. E. Bakan, Y. J. Sohn, and R. Vaßen, "Metastable to Stable Phase Transformation in Atmospheric Plasma Sprayed Yb-silicate Coating During Post-heat Treatment," *Scripta Materialia* 225 (2023): 115169, https://doi.org/10.1016/j.scriptamat.2022.115169.

29. E. Bakan, D. E. Mack, S. Lobe, D. Koch, and R. Vaßen, "An Investigation on Burner Rig Testing of Environmental Barrier Coatings for Aerospace Applications," *Journal of the European Ceramic Society* 40, no. 15 (2020): 6236–6240, https://doi.org/10.1016/j.jeurceramsoc.2020.06.016.

30. M. D. Thouless, "Cracking and Delamination of Coatings," *Journal of Vacuum Science & Technology A: Vacuum, Surfaces, and Films* 9, no. 4 (1991): 2510–2515, https://doi.org/10.1116/1.577265.

31. S. V. Shinde, E. J. Gildersleeve V, C. A. Johnson, and S. Sampath, "Segmentation Crack Formation Dynamics During Air Plasma Spraying of Zirconia," *Acta Materialia* 183 (2020): 196–206, https://doi.org/10.1016/j.actamat.2019.10.052.

32. B. T. Richards, K. A. Young, F. de Francqueville, S. Sehr, M. R. Begley, and H. N. Wadley, "Response of Ytterbium Disilicate–silicon Environmental Barrier Coatings to Thermal Cycling in Water Vapor," *Acta Materialia* 106 (2016): 1–14, https://doi.org/10.1016/j.actamat.2015.12.053.

33. E. Bakan, V. E. J. Gildersleeve, and R. Vaßen, "Toward Highly Dense Yb-Silicate Microstructures Deposited by Air Plasma Spray for Environmental Barrier Coating Applications I: Influence of Local Deposition Rate," *Journal of Thermal Spray Technology* 34, no. 5 (2025): 1985–1994.

34. G. Mauer, A. Guignard, R. Vaßen, and D. Stöver, "Process Diagnostics in Suspension Plasma Spraying," *Surface and Coatings Technology* 205, no. 4 (2010): 961–966, https://doi.org/10.1016/j.surfcoat.2010.03.007.

35. F. Traeger, R. Vaßen, K. H. Rauwald, and D. Stöver, "Thermal Cycling Setup for Testing Thermal Barrier Coatings," *Advanced Engineering Materials* 5, no. 6 (2003): 429–432, https://doi.org/10.1002/adem.200300337.

36. N. Schlegel, S. Ebert, G. Mauer, and R. Vassen, "Columnar-Structured Mg-Al-Spinel Thermal Barrier Coatings (TBCs) by Suspension Plasma Spraying (SPS)," *Journal of Thermal Spray Technology* 24, no. 1-2 (2015): 144–151.

37. X. Zhang, B. Xu, F. Xuan, H. Wang, Y. Wu, and S. Tu, "Statistical Analyses of Porosity Variations in Plasma-sprayed Ni-based Coatings," *Journal of Alloys and Compounds* 467, no. 1-2 (2009): 501–508, https://doi.org/10.1016/j.jallcom.2007.12.083.

38. D. L. Sahagian and A. A. Proussevitch, "3D particle Size Distributions From 2D Observations: Stereology for Natural Applications," *Journal of Volcanology and Geothermal Research* 84, no. 3-4 (1998): 173–196, https://doi.org/10.1016/S0377-0273(98)00043-2.

39. G. Montavon and G. Antou, "Quantifying Thermal Spray Coating Architecture by Stereological Protocols: Part I. A Historical Perspective," *Journal of Thermal Spray Technology* 16, no. 1 (2007): 6–14, https://doi.org/10.1007/s11666-007-9017-8.

40. "Introduction to Stereologic Principles," in Quantitative Methods in Morphology/Quantitative Methoden in der Morphologie: Proceedings of the Symposium on Quantitative Methods in Morphology held on August 10, 1965, during the Eigth International Congress of Anatomists in, Wiesbaden, Germany (Springer, 1967).

41. M. Gockenbach and K. Schmidtke, "Newton's Law of Heating and the Heat Equation," *Involve, A Journal of Mathematics* 2, no. 4 (2009): 419–437.

42. K. Ramadan and P. B. Butler, "Analysis of Particle Dynamics and Heat Transfer in Detonation Thermal Spraying Systems," *Journal of Thermal Spray Technology* 13, no. 2 (2004): 248–264, https://doi.org/10.1361/10599630419373.

43. U. Besson, "The History of the Cooling Law: When the Search for Simplicity Can be an Obstacle," *Science & Education* 21 (2012): 1085–1110, https://doi.org/10.1007/s11191-010-9324-1.

44. E. Garcia, H. F. Garces, L. R. Turcer, H. Bale, N. P. Padture, and S. Sampath, "Crystallization Behavior of Air-plasma-sprayed Ytterbium-silicate-based Environmental Barrier Coatings," *Journal of the European Ceramic Society* 41, no. 6 (2021): 3696–3705, https://doi.org/10.1016/j.jeurceramsoc.2020.12.051.

45. R. Vaßen, E. Bakan, D. Sebold, and Y. J. Sohn, "Correlation of Process Conditions, Porosity Levels and Crystallinity in Atmospherically Plasma Sprayed Yb2Si2O7 Environmental Barrier Coatings," *Journal of Composites Science* 5, no. 8 (2021): 198.

46. C. Delbos, J. Fazilleau, V. Rat, J.-F. Coudert, P. Fauchais, and B. Pateyron, "Phenomena Involved in Suspension Plasma Spraying Part 2: Zirconia Particle Treatment and Coating Formation," *Plasma Chemistry and Plasma Processing* 26, no. 4 (2006): 393–414, https://doi.org/10.1007/s11090-006-9020-8.

47. Y. Wang, Q. Fu, H. Dong, et al., "CMAS Corrosion Behavior of Interface for EB-PVD $Gd_2Zr_2O_7$/YSZ Thermal Barrier Coatings," *Materials Today Communications* 41 (2024): 110756, https://doi.org/10.1016/j.mtcomm.2024.110756.

48. E. J. Opila, J. L. Smialek, R. C. Robinson, D. S. Fox, and N. S. Jacobson, "SiC Recession Caused by SiO_2 Scale Volatility Under Combustion Conditions: II, Thermodynamics and Gaseous-Diffusion Model," *Journal of the American Ceramic Society* 82, no. 7 (1999): 1826–1834, https://doi.org/10.1111/j.1151-2916.1999.tb02005.x.

49. G. C. C. Costa and N. S. Jacobson, "Mass Spectrometric Measurements of the Silica Activity in the Yb_2O_3–SiO_2 System and Implications to Assess the Degradation of Silicate-based Coatings in Combustion Environments," *Journal of the European Ceramic Society* 35, no. 15 (2015): 4259–4267, https://doi.org/10.1016/j.jeurceramsoc.2015.07.019.

50. J. V. Heberlein, P. Fauchais, and M. I. Boulos, *Thermal Spray Fundamental: From Powder to Part* (Springer Nature, 2014).

15512916, 2026, 7, Downloaded from https://ceramics.onlinelibrary.wiley.com/doi/10.1111/jace.70976 by Forschungszentrum Jülich GmbH Research Center, Wiley Online Library on [12/08/2026]. See the Terms and Conditions (https://onlinelibrary.wiley.com/terms-and-conditions) on Wiley Online Library for rules of use; OA articles are governed by the applicable Creative Commons License